Structures, Phase Fields, and Mixed Protonic−Electronic Conductivity of Ba-Deficient, Pr-Substituted BaZr$_{0.7}$Ce$_{0.2}$Y$_{0.1}$O$_{3−\delta}$

Gemma Heras-Juaristi,[†] Ulises Amador,[‡] Julio Romero de Paz,[§] Rodolfo O. Fuentes,[||] Adilson L. Chinelatto,[⊥] Clemens Ritter,[#] Duncan P. Fagg,[∇] Domingo Pérez-Coll,[†] and Glenn C. Mather*,[†]

[†]Instituto de Cerámica y Vidrio, CSIC, Cantoblanco, 28049 Madrid, Spain

[‡]Facultad de Farmacia, Departamento de Química, Universidad CEU-San Pablo, Boadilla del Monte, Madrid 28668, Spain

[§]C.A.I. Técnicas Físicas, Facultad de Ciencias Físicas, Universidad Complutense, 28040 Madrid, Spain

[||]Departamento de Física de la Materia Condensada, CNEA, Av. Gral. Paz 1499, 1650 Buenos Aires, Argentina

[⊥]Departamento de Engenharia de Materiais, Universidade Estadual de Ponta Grossa, Av. Gal. Carlos Cavalcanti, 4748, 84030-900 Ponta Grossa, PR, Brazil

[#]Institut Laue-Langevin, 71 Avenue des Martyrs, Grenoble 38042, France

[∇]Department of Mechanical Engineering, University of Aveiro, 3810-193 Aveiro, Portugal

ABSTRACT: The BaZr$_{0.7}$Ce$_{0.2}$Y$_{0.1}$O$_{3−\delta}$−BaPrO$_{3−\delta}$ perovskite system, of interest for high-temperature electrochemical applications involving mixed protonic−electronic conductivity, forms a solid-solution with a wide interval of Ba substoichiometry in the range Ba(Ce$_{0.2}$Zr$_{0.7}$)$_{1−x}$Pr$_x$Y$_{0.1}$O$_{3−\delta}$, $0 \leq x \leq 1$. Structural phase transitions mapped as a function of temperature and composition by high-resolution neutron powder diffraction and synchrotron X-ray diffraction reveal higher symmetry for lower Pr content and higher temperatures, with the largest stability field observed for rhombohedral symmetry (space group, $R\bar{3}c$). Rietveld refinement, supported by magnetic-susceptibility measurements, indicates that partitioning of the B-site cations over the A and B perovskite sites compensates Ba substoichiometry in preference to A-site vacancy formation and that multiple cations are distributed over both sites. Electron−hole

transport dominates electrical conductivity in both wet and dry oxidizing conditions, with total conductivity reaching a value of ∼0.5 S cm$^{−1}$ for the $x = 1$ end-member in dry air at 1173 K. Higher electrical conductivity and the displacement of oxygen loss to higher temperatures with increasing Pr content both reflect the role of Pr in promoting hole formation at the expense of oxygen vacancies. In more reducing conditions (N$_2$) and at low Pr contents, conductivity is higher in humidified atmospheres (∼0.023 atm pH$_2$O) indicating a protonic contribution to transport, whereas the greater electron−hole conductivity with increasing Pr content results in lower conductivity in humidified N$_2$ due to the creation of protonic defects and the consumption of holes.
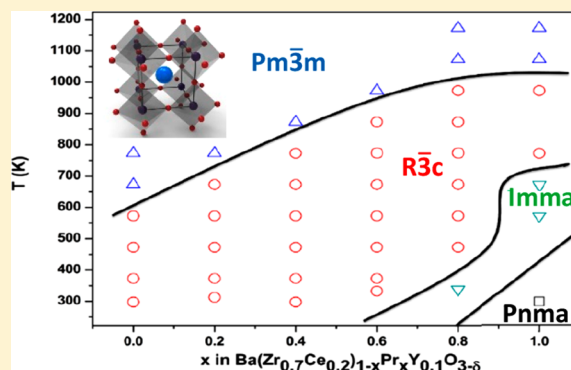
INTRODUCTION

The development of mixed-conducting protonic−electronic ceramic materials is of considerable interest for a number of high-temperature electrochemical applications involving hydrogen. Barium cerium−zirconate solid-solutions with the perovskite (ABO$_3$) structure have emerged as strong candidate materials for electrochemical membranes, with much focus on the composition BaZr$_{0.7}$Ce$_{0.2}$Y$_{0.1}$O$_{3−\delta}$ (BZCY72),[1,2] which provides both good stability and moderately high proton transport.[3]

The conversion of hydrogen to electrical energy may take place in protonic ceramic fuel cells (PCFCs) which operate within an intermediate temperature range (773−973 K) employing BZCY72 or related solid-solution members as

electrolytes. Lower temperatures are more advantageous for long-term stability, balance-of-plant costs, and miniaturization; however, with lower temperature, large overpotentials are encountered at the electrode−electrolyte interface due to slower reaction kinetics. The role of the cathode is, therefore, crucial to fuel efficiency in this temperature range. The influence of proton and oxide-ion conductivities on cathode performance in PCFCs has not been clearly established. Although different electrode designs have been experimented with, it is nevertheless apparent that high electron (or electron hole) transport is essential.

One strategy to improve cathode performance is through the introduction of greater electronic conductivity in a proton-conducting phase. For example, Fabbri et al. induced higher electronic transport in $BaZr_{0.9}Y_{0.1}O_{3-\delta}$ on substituting Zr by Pr,[4] but the conductivity was still too low for application as a single-phase cathode. In contrast, the approach of substituting electronically conducting perovskite SOFC cathode compositions with cations that may induce proton transport, in particular Zr-doped $Ba(Co, Fe, Y)O_{3-\delta}$,[5,6] has led to very low polarization resistances for both PCFCs and oxide-ion-based solid oxide fuel cells (SOFCs). Similarly, mixed protonic–electronic conduction is required in membrane technologies for hydrogen separation, which may be coupled with useful reactions such as the reduction of CO_2[7] or methane dehydroaromatization,[8] whereby natural gas is converted in a nonoxidative process to aromatics.

Praseodymium is an interesting dopant for perovskite cerates and zirconates as it can, in principle, occupy both A- and B-sites,[9] increase sinterability,[10] and augment electronic conductivity.[11,12] Although compositions with low levels of Pr doping are reported to exhibit good stability,[10] Pr-rich perovskites are associated with poor stability in wet and reducing gases.[12−14] We have recently studied the effects of Pr substitution in BZCY72, finding that substitution of Zr/Ce with Pr led to higher electronic conductivity and a number of symmetry changes dependent on Pr content and temperature.[15] Of interest in this and other recent related studies of the Pr-substituted $BaZrO_3$ system[9,16] was the finding that Pr resides exclusively on the perovskite B-site in the IV oxidation state, despite the fact that ion site size requirements indicate that Pr^{3+} is much more likely to occupy the A-site. Mixed Pr oxidation states were, therefore, discounted as the origin of the enhanced thermally activated electronic conductivity. It was also reported that the type of charge-compensation mechanism for Pr substitution is highly dependent on the Pr concentration.

In general, A-site deficiency is a widely adopted strategy for tailoring the defect chemistry and doping mechanisms in technologically relevant perovskites in order to improve the physicochemical properties.[17−20] A-site substoichiometry in Y-doped $BaZrO_{3-\delta}$ (BZY) arising from Ba evaporation on sintering is considered to be compensated by partitioning of the Y dopant on the A-site leading to a decrease in proton conductivity and unit-cell constant.[21] On the other hand, Ba deficiency in the $BaCeO_3$-based phase was recently reported to lower grain-boundary resistances and improve stability by cleaning the grain boundaries of an amorphous nanometer-thick barium oxide layer.[22] The effects on electrical properties and defect chemistry of engineering compositions with potential for either A-site vacancy formation or dopant partitioning in Pr-doped systems have been studied for a limited range of A-site nonstoichiometry in the case of $Ba_{0.95}Zr_{0.8}Pr_{0.2}O_{3-\delta}$, revealing redistribution of Pr over both A- and B-sites and partial reduction of Pr^{4+} to Pr^{3+}, especially at high temperatures in reducing conditions.[9] The combined effects of A-site deficiency and dopant partitioning often occur unintentionally as a result of high-temperature firing but may also be extremely useful for engineering transport, stability, and electrocatalytic properties.

In this paper, continuing our exploration of the BZCY72-$BaPrO_3$ system with potential application as mixed protonic, oxide-ionic, and electronic conductors for high-temperature electrochemical devices, we report the synthesis of the solid-solution $Ba(Zr_{0.7}Ce_{0.2})_{1−x}Pr_xY_{0.1}O_{3-\delta}$ in which Ba substoichiometry increases with x. We map the structural phase transitions occurring in the $Ba(Zr_{0.7}Ce_{0.2})_{1−x}Pr_xY_{0.1}O_{3-\delta}$ system as a function of temperature and composition by high-resolution neutron powder diffraction supplemented by synchrotron radiation X-ray diffraction (SR-XRD) in different atmospheres. The structural information, complemented by magnetic-susceptibility measurements to assess the Pr oxidation state and the consequent Pr-site distribution, is employed to analyze the effects of Ba substoichiometry and Pr substitution on electrical conductivity, determined in dry and humidified air and N_2 atmosphere by impedance spectroscopy.

■ EXPERIMENTAL SECTION

Members of the solid-solution series $Ba(Zr_{0.7}Ce_{0.2})_{1−x}Pr_xY_{0.1}O_{3-\delta}$ (x = 0, 0.2, 0.4, 0.6, 0.8, 1.0) were synthesized by a citrate−nitrate process based on the Pechini method. The water content of the nitrate precursors was first determined by thermogravimetry in air with an SDT Q600 instrument. The appropriate stoichiometric ratio of nitrates was added to deionized water heated at 323 K on a hot plate in the order $Ba(NO_3)_2 \cdot xH_2O$, $ZrO(NO_3)_2 \cdot xH_2O$, $Ce(NO_3)_3 \cdot xH_2O$, $Y(NO_3)_3 \cdot xH_2O$, and $Pr(NO_3)_3 \cdot xH_2O$. On obtaining a transparent green solution, the temperature was first raised in the range 333−353 K for ~2 h then subsequently to >363 K for 4−5 h, and finally to above 373 K for over 12 h. The obtained dark-brown polymerized complex was then pyrolyzed in an oven at 623 K for 4 h. The resulting polymeric precursor was heated at 873 K for 4 h, milled, and heat treated at 1373 K for a further 4 h to remove any remaining organic product, before attrition milling in Teflon vials and sieving (100 μm). Phase analysis and structural characterization were performed on powders prepared by uniaxially pressing the as-prepared powder into 10 mm diameter cylindrical pellets, covered with sacrificial powder of the same composition and firing in the range 1623−1773 K for 4 h. The pellets were then crushed and milled in an agate mortar and pestle in acetone. Pellets were prepared for electrochemical and magnetic measurements after treatment at 1373 K employing a further heat treatment at 1523 K for 24 h with intermediate grinding followed by attrition milling and sieving (100 μm) prior to sintering the pressed powders at 1923 K for 4−8 h.

Phase analysis was initially performed by powder X-ray diffraction (XRD) on a Bruker D8 high-resolution diffractometer, using monochromatic Cu Kα_1 radiation (λ = 1.5406 Å). Neutron powder diffraction (NPD) measurements were conducted on the high-resolution D2B diffractometer at the Institut Laue Langevin (Grenoble, France) on heating within a temperature range 299−1173 K. A Ge monochromator was employed to select a monochromatic beam wavelength of 1.594 Å from the primary beam. Synchrotron radiation X-ray diffraction (SR-XRD) patterns were recorded on samples mounted on a ceramic sample holder and heated in a furnace in the range 773−1173 K in controlled atmospheres of dry and wet synthetic air (flow rate, 50 mL min$^{−1}$) and dry N_2 (100 mL min$^{−1}$) at the D10B-XPD beamline of the National Synchrotron Light Laboratory (LNLS, Campinas, Brazil). The X-ray wavelength was set to 1.54915 Å. Data in the range 20° ≤ 2θ ≤ 90° were collected in step-scanning mode, with a step length of 0.005° and a step-counting time of 2 s. Samples were heated at a rate of 10 K min$^{−1}$, and a dwell time of 10 min was employed at each temperature before performing the XRD scan. NIST SRM 640c Si powder was used as the standard for the instrumental broadening correction. Structural refinements of the NPD and SR-XRD data were performed by the Rietveld method with the Fullprof program.[23]

The temperature dependence of the molar magnetic-susceptibility χ of the series was determined with a superconducting quantum interference device magnetometer (Quantum Design, model MPMS-XL). Polycrystalline samples were measured according to the procedure described elsewhere.[15]

Thermogravimetric analysis (TGA) was performed with an initial heating−cooling cycle in synthetic air on heating at 10 K min$^{−1}$ in the

Table 1. Phase Compositions and Possible Compensation Mechanisms in the $Ba(Zr_{0.7}Ce_{0.2})_{1-x}Pr_xY_{0.1}O_{3-\delta}$ Series

x	nominal composition	vacancy mechanism	Pr partition mechanism	multiple-cation partition mechansim
0	$BaZr_{0.7}Ce_{0.2}Y_{0.1}O_{3-\delta}$			
0.2	$Ba(Zr_{0.56}Ce_{0.16}Pr_{0.2}Y_{0.1})O_{3-\delta}$	$Ba_{0.980}(Zr_{0.549}Ce_{0.157}Pr_{0.196}Y_{0.098})O_{3-\delta}$	$(Ba_{0.990}Pr_{0.010})(Zr_{0.554}Ce_{0.158}Pr_{0.188}Y_{0.099})O_{3-\delta}$	$(Ba_{0.990}Y_{0.010})(Zr_{0.554}Ce_{0.158}Pr_{0.196}Y_{0.091})O_{3-\delta}$
0.4	$Ba(Zr_{0.42}Ce_{0.12}Pr_{0.4}Y_{0.1})O_{3-\delta}$	$Ba_{0.962}(Zr_{0.404}Ce_{0.115}Pr_{0.385}Y_{0.096})O_{3-\delta}$	$(Ba_{0.980}Pr_{0.020})(Zr_{0.412}Ce_{0.118}Pr_{0.373}Y_{0.098})O_{3-\delta}$	$(Ba_{0.980}Y_{0.020})(Zr_{0.412}Ce_{0.118}Pr_{0.395}Y_{0.078})O_{3-\delta}$
0.6	$Ba(Zr_{0.28}Ce_{0.08}Pr_{0.6}Y_{0.1})O_{3-\delta}$	$Ba_{0.943}(Zr_{0.264}Ce_{0.075}Pr_{0.566}Y_{0.094})O_{3-\delta}$	$(Ba_{0.971}Pr_{0.029})(Zr_{0272}Ce_{0.078}Pr_{0.553}Y_{0.097})O_{3-\delta}$	$(Ba_{0.971}Pr_{0.006}Y_{0.023})(Zr_{0.272}Ce_{0.078}Pr_{0.576}Y_{0.074})O_{3-\delta}$
0.8	$Ba(Zr_{0.14}Ce_{0.04}Pr_{0.8}Y_{0.1})O_{3-\delta}$	$Ba_{0.926}(Zr_{0.130}Ce_{0.037}Pr_{0.741}Y_{0.093})O_{3-\delta}$	$(Ba_{0.962}Pr_{0.038})(Zr_{0.135}Ce_{0.038}Pr_{0.731}Y_{0.096})O_{3-\delta}$	$(Ba_{0.962}Pr_{0.023}Y_{0.015})(Zr_{0.135}Ce_{0.038}Pr_{0.746}Y_{0.081})O_{3-\delta}$
1.0	$Ba(PrY_{0.1})O_{3-\delta}$	$Ba_{0.909}(Pr_{0.909}Y_{0.091})O_{3-\delta}$	$(Ba_{0.952}Pr_{0.048})(Pr_{0.905}Y_{0.095})O_{3-\delta}$	$(Ba_{0.952}Pr_{0.031}Y_{0.017})(Pr_{0.922}Y_{0.078})O_{3-\delta}$

temperature range 298−1303 K followed by a further heating cycle in 100% CO_2 with a heating rate of 5 K min^{-1} to check stability versus the formation of $BaCO_3$.

Cylindrical pellets were prepared for electrical measurements by coating the faces with Heraeus Pt paste (CL11-5349) and firing at 1173 K for 1 h. Impedance spectroscopy was employed to determine conductivity as a function of temperature on cooling in steps of 50 K in the temperature range 423−1173 K employing an Autolab PGStat302N-FRA2 instrument operating over the frequency range $0.1 \leq f \leq 10^6$ Hz with a signal amplitude of 50 mV in potentiostatic mode. Measurements were registered in dry atmospheres of air and N_2 on feeding the gas directly through a drying column containing a commercial moisture trap of aluminosilicate- and zeolite-based beads (Supelco). For wet air and N_2 atmospheres, the gas was first bubbled through KBr-saturated water at room temperature (RT) to provide a water content of ∼0.023 atm. Analysis of impedance spectra was performed with the Zview 2.9c software (Scribner Associates) by fitting the data to appropriate equivalent circuits in order to resolve the impedance response into bulk, grain-boundary, and electrode contributions.
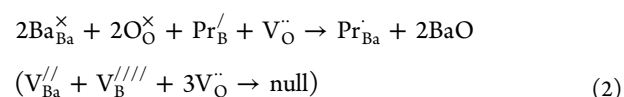
RESULTS AND DISCUSSION

Phase Formation, Phase Fields, and Cation Distribution. Solid-solution formation was confirmed by XRD for the complete $Ba(Zr_{0.7}Ce_{0.2})_{1-x}Pr_xY_{0.1}O_{3-\delta}$ series on sintering at 1698 K for 4 h; the nominal compositions of the series are listed in Table 1 (column 1). Peak splitting for the series was enhanced with increasing Pr content indicating more complex structural detail associated with octahedral tilting. High-resolution neutron powder diffraction is most useful in the analysis of the concerted oxygen movements in these tilted perovskites and, in turn, for the precise determination of space group due to the much higher neutron scattering factor of oxygen in comparison to that of X-rays, as has been recently demonstrated for BZCY72[24] and the related Ba-stoichiometric solid-solution.[15]

Superlattice reflections in the NPD patterns confirmed that the title series was distorted from the cubic perovskite aristotype, and these were indexed in accordance with the method of Glazer[25] and Woodward and Reaney.[26] The 1/2{ooo} pattern (where "o" represents an odd-number index) of the simple cubic unit cell observed for both the present and sister series[27] is compatible with uniquely antiphase tilting of the BO_6 octahedra, with possible space groups $I4/mcm$, $Imma$, and $R\bar{3}c$. The final symmetry was determined through analysis of the superlattice reflections originating from the distortion of the aristotype and inspection of the corresponding refinement quality criteria.

The NPD data were fitted in the temperature range from RT to 338 K using the appropriate orthorhombic, rhombohedral, or cubic structural model with both an A-site-vacancy mechanism (Kröger−Vink notation)

$$Ba_{Ba}^{\times} + O_O^{\times} \rightarrow V_{Ba}^{//} + V_O^{\cdot\cdot} + BaO \qquad (1)$$
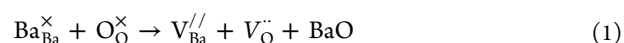
and a partition mechanism involving distribution of the B-site species over both A- and B-sites,[20] expressed below for the case of Pr:

$$2Ba_{Ba}^{\times} + 2O_O^{\times} + Pr_B^{/} + V_O^{\cdot\cdot} \rightarrow Pr_{Ba}^{\cdot} + 2BaO$$

$$(V_{Ba}^{//} + V_B^{////} + 3V_O^{\cdot\cdot} \rightarrow null) \qquad (2)$$

Note that this mechanism is preceded by the formation of a Pr^{3+} species

$$2Pr_B^{\times} + O_O^{\times} \rightarrow 2Pr_B^{/} + V_O^{\cdot\cdot} + \frac{1}{2}O_2 \qquad (3)$$
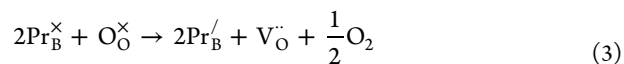
Although reduction creates oxygen vacancies, the overall dopant partitioning mechanism (eqs 2 and 3) leads to consumption of oxygen vacancies whereas they are created via the A-site vacancy mechanism (eq 1). Further compensation regimes, such as occupation of the A-site by a B-site cation and concomitant formation of either B-site cation vacancies or oxygen interstitials, were discounted on the basis of their expected improbably high energy penalties. Cation ordering on either cation site was also disregarded due to the absence of associated supercell reflections. The refinement quality criteria on refining according to either the A-site vacancy or partition mechanism with the compositions indicated in Table 1 (columns 2 and 3) generally improved for the latter, indicating full A-site occupancy. This improvement is shown as a percentage of the difference between compensation and vacancy mechanisms over the vacancy mechanism for the R_{Bragg} and χ^2 quality refinement parameters in Figure 1. In addition to illustrating the improved refinement with a partition mechanism as opposed to a vacancy mechanism, the figure also reveals a further slight improvement in refinements when Y or both Y and Pr occupy the A-site according to the compositions listed in Table 1, column 4 (discussed below with regard to the magnetic data). There is, in general, a greater difference observed for the Bragg R-factor between the vacancy mechanism and the two partition mechanisms (Table 1) for later members of the series in Figure 1 due to the greater difference in site occupancies with increasing Pr content.

In order to clarify the oxidation state and site distribution of the paramagnetic praseodymium atoms in the $Ba(Zr_{0.7}Ce_{0.2})_{1-x}Pr_xY_{0.1}O_{3-\delta}$ series, we compared the magnetism of the Pr-rich end-member ($x = 1$) with that of nominally Ba-stoichiometric $BaPr_{0.9}Y_{0.1}O_{3-\delta}$.[15] Note that both phases have similar nominal composition with respect to the B-site cations. It is well-known that the theoretical value for a free Pr^{4+} cation in its $J = \frac{5}{2}$ ground state, 2.54 μ_B, is largely reduced when it is
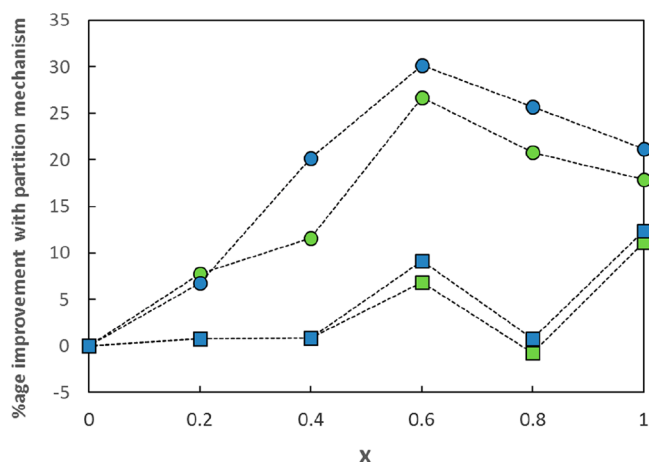
Figure 1. Percentage improvement of the Rietveld refinement criteria R_{Bragg} $\left(\left(\frac{R_{B,vac} - R_{B,part}}{R_{B,vac}} \right) \times 100\% \right)$, shown as circles, and χ^2, shown as squares, of the $Ba(Zr_{0.7}Ce_{0.2})_{1-x}Pr_xY_{0.1}O_{3-\delta}$ series on comparison of the partition mechanism ($R_{B,part}$, χ^2_{part}) with the vacancy mechanism ($R_{B,vac}$, χ^2_{vac}). Results employing the partition mechanism of charge compensation with only Pr are shown in green, and those with a multiple-cation partition mechanism are shown in blue; the employed compositions are listed in Table 1. Data were determined from neutron diffraction (ND) at 573 K.

Figure 2. Thermal variation of the magnetic-susceptibility for member $x = 1$ of the $Ba(Zr_{0.7}Ce_{0.2})_{1-x}Pr_xY_{0.1}O_{3-\delta}$ series in an applied field of 100 mT. The solid black line is a guide for the eye. The inset shows the corresponding inverse magnetic-susceptibility versus temperature plot, and the solid red line is the best fit ($r^2 = 0.99999$) of the data obtained between 30 and 300 K to the χ^{-1} function where $\chi = \frac{C}{T - \theta} + \chi_0$.

located in an octahedral site, such as the B-site of the perovskite-type structure; reduced magnetic-moment values usually range from 0.68 μ_B for $BaPrO_3$[28] to 1.57 μ_B for $SrPrO_3$.[29] The rather low magnetic-moment value ((0.65 ± 0.02) μ_B) determined for the paramagnetic praseodymium ion of $BaPr_{0.9}Y_{0.1}O_{3-\delta}$ strongly supported a B-site location and +4 oxidation state for Pr in this case.[15] Further evidence for this was the weak ferromagnetism observed below 9.5 K due to long-range antiferromagnetic ordering of Pr^{4+} moments, as in the case of $BaPrO_3$ oxide with a Néel temperature of T_N = 11.6 K;[30,31] the partial substitution of praseodymium by yttrium accounts for the slightly different ordering temperatures between the two phases.

The temperature dependence of the magnetic-susceptibility χ obtained for the $x = 1$ member of the current series is shown in Figure 2. The increase of χ as temperature decreases from RT down to 30 K corresponds to paramagnetic behavior described well by the modified Curie−Weiss law $\chi = \frac{C}{T-\theta} + \chi_0$, where the Curie constant (C), the Weiss temperature (θ), and the temperature-independent paramagnetism (χ_0) take the values $1.059 \times 10^{-1} \pm 2 \times 10^{-4}$ emu K mol Pr^{-1} Oe^{-1}, -21.1 ± 0.1 K, and $6.228 \times 10^{-4} \pm 5 \times 10^{-7}$ emu mol Pr^{-1} Oe^{-1}, respectively.

The sharp increase of χ observed at 9.5 K indicates an antiferromagnetic transition with a weak ferromagnetic component, analogous to that occurring in $BaPrO_3$.[30,31] The magnetic moment calculated from the C value ($\mu = \sqrt{8C}$) is (0.92 ± 0.01) μ_B, which is significantly larger than our reference value of 0.65 μ_B determined for $BaPr_{0.9}Y_{0.1}O_{3-\delta}$.[15] In contrast, both this phase and the $x = 1$ member of the present series exhibit an identical ordering temperature (T_N = 9.5 K), indicating that both the composition of the B sublattices and the effect of crystal field on Pr^{4+} must be very similar for the two compositions.[32−34] In light of this scenario, and with consideration of ion site size requirements, it follows that the
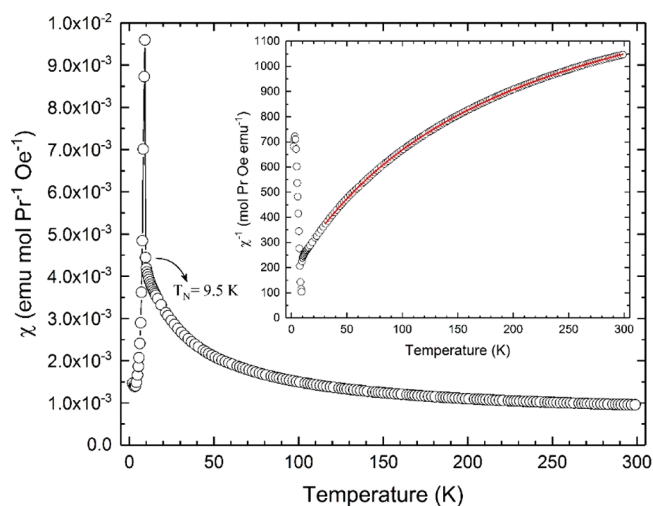
presence of Pr^{3+} atoms on the perovskite A-site accounts for the increment of the magnetic moment in the title series, assuming that the magnetic interactions involving Pr on the B-site remain unchanged. The magnetic data strongly support, therefore, the conclusions of the Rietveld refinement analysis that partitioning of Pr over the A and B perovskite sites compensates for, at least in part, barium substoichiometry.

Nevertheless, the experimental magnetic moment for the $x = 1$ end-member was found to be slightly lower than the theoretical value for a scenario with full Pr partitioning (Table 1, column 3), and therefore, the full A-site occupancy must imply not only that Pr partially occupies the A-site but also that diamagnetic Y^{3+} cations are also distributed over both sites. The Rietveld refinements were repeated on the basis of a multiple-cation partitioning (Table 1, column 4), leading to further improvement in the refinement quality criteria (blue symbols, Figure 1). Cerium partitioning over the A and B perovskite sites was discounted on the basis of the higher energy required for the reduction of Ce^{4+} to Ce^{3+} as contrasted with the reduction of Pr^{4+} to Pr^{3+}.[35]

We note that, in other A-site-deficient series, anomalous variations in unit-cell parameters with compositions are observed.[36] In the case of $Sr_{1-x}Ce_{0.9}Yb_{0.1}O_{3-\delta}$, this was attributed to a change in compensation mechanism for A-site vacancy to dopant partitioning with increasing A-site cation deficiency.[20] In the present study, lattice parameters were linear with composition (not shown) and the Rietveld results indicate that the compensation mechanism is unchanged throughout the series. Refinements were improved on employment of anisotropic temperature factors. Final structural parameters of selected phases at low temperatures (from RT to 338 K) are listed in Table 2. The corresponding observed and calculated NPD patterns are shown in Figure 3.

The phase fields of the series as a function of temperature and composition (x) as determined from the NPD data, Figure 4, reflect the increasing tilting of the BO_6 octahedra with increasing x and lower temperature.

Table 2. Structural Parameters, Interatomic Distances, and Agreement Factors for Selected Members of the $Ba(Zr_{0.7}Ce_{0.2})_{1-x}Pr_xY_{0.1}O_{3-\delta}$ Solid-Solution Series Obtained from NPD Data

	0.2 ($R\bar{3}c$)[a,c]	0.4 ($R\bar{3}c$)[a,d]	0.6 ($R\bar{3}c$)[a,e]	0.8 (*Imma*)[b,f]
a (Å)	6.0529(4)	6.0913(2)	6.1264(2)	6.1425(2)
b (Å)	6.0529(4)	6.0913(2)	6.1264(2)	8.6684(2)
c (Å)	14.802(2)	14.8588(9)	14.9327(7)	6.1790(2)
V (Å³)	469.64(7)	477.45(4)	485.38(3)	329.01(2)
A position[g]	6a	6a	6a	4e
z				0.0017(6)
$U_{iso} \times 100$ (Å²)	1.10(4)	1.17(5)	1.14(4)	1.03(4)
B position[g]	6b	6b	6b	4b
$U_{iso} \times 100$ (Å²)	0.72(4)	0.64(4)	0.55(4)	0.65(3)
O(1) position	18e	18e	18e	4e
x	0.4673(3)	0.4578(2)	0.4527(2)	
z				−0.0649(4)
occ	2.97(2)	3.02(2)	2.97(2)	0.97(1)
$U_{iso} \times 100$ (Å²)	2.3(1)	2.3(1)	2.3(1)	1.8(1)
O(2) position				8g
y				−0.0338(2)
occ				2.07(2)
$U_{iso} \times 100$ (Å²)				2.7(1)
		Selected Distances (Å)		
Ba−O(1)	3.224(1) × 3	3.298(1) × 3	3.3530(8) × 3	3.0987(6) × 2
	2.793(1) × 3	2.793(1) × 3	2.7734(8) × 3	2.699(4)
	3.048(1) × 6	3.048(1) × 6	3.0669(9) × 6	3.480(4)
Ba−O(2)				3.291(2) × 4
				2.868(2) × 4
av Ba−O	3.073(1)	3.092(1)	3.0644(8)	3.084(2)
B−O(1)	2.1480(9) × 6	2.1654(9) × 6	2.1818(6) × 6	2.2039(5) × 2
B−O(2)				2.1978(2) × 4
av B−O	2.1480(9)	2.1654(9)	2.1818(6)	2.1998(3)
t-factor[h]	1.0116	1.0097	0.9932	0.9913

[a]Space group $R\bar{3}c$ (No. 62): 6a (001), 6b (000), 18e (x01). [b]Space group *Imma* (No. 74): 4b ($0^1/_2^1/_2$), 4e (01z), 8g (1y0). [c]T = 313 K; χ^2 = 1.26, R_{exp} = 3.59%, R_{wp} = 4.02%, R_B = 1.42%, $\rho_{(cryst)}$: 6.220(1) g/cm³. [d]T = 299 K; χ^2 = 1.22, R_{exp} = 3.48%, R_{wp} = 3.83%, R_B = 1.62%, $\rho_{(cryst)}$: 6.291(1) g/cm³. [e]T = 333 K; χ^2 = 1.42, R_{exp} = 4.05%, R_{wp} = 4.82%, R_B = 1.91%, $\rho_{(cryst)}$: 6.461(1) g/cm³. [f]T = 338 K; χ^2 = 1.23, R_{exp} = 4.07%, R_{wp} = 4.52%, R_B = 2.11%, $\rho_{(cryst)}$: 6.463(x) g/cm³. [g]A and B cation occupancies are those of the multiple-cation partition mechanism, Table 1. [h]Goldschmidt tolerance factor $t = \frac{d(A-O)}{\sqrt{2}\,d(B-O)}$.

With greater Pr content, the Goldschmidt tolerance factor is lower due to the presence of the larger Pr^{4+} cation on the B-site in comparison to the average ionic radii of the substituted Zr/Ce cations. The presence of the smaller B-site cations in comparison to Ba on the A-site will also lower the tolerance factor. The stress associated with mismatch of the A−O and B−O bond lengths is partially alleviated with increasing temperature leading to higher symmetry structures. The transition to cubic symmetry which is displaced to higher temperature with increasing Pr content may be followed by the octahedral tilt angle (φ) calculated from the refined oxygen position of the hexagonal cell[37] and shown in Figure 5 for x = 0.8.

The pseudocubic lattice parameters of the title series in the range RT to 1173 K determined from both NPD and SR-XRD data are shown in Figure 6. The behavior in air (SR-XRD data) is similar to that of the BZCY72 end-member[38] and the recently studied Ba-stoichiometric series,[15] with a greater expansion in the low-temperature range followed by a return to purely thermal expansion observed for the Pr-lean series members as temperature increases. This nonlinearity was attributed to loss of water present in the as-prepared materials and is observed for similar proton-conducting perovskites.[38,39] Analogous to the Ba-stoichiometric series, later members

exhibit greater linearity of lattice parameter with temperature, although deviations occur on undergoing a first-order phase transition from orthorhombic to rhombohedral symmetry. However, data for the Pr-containing members x = 0.2 and 0.4 collected in low vacuum (ND) deviate somewhat from this previously observed behavior in that, in the range where the deviation from the expected thermal-expansion trend is most pronounced, the lattice parameter is lower, and then converges with the expected thermal expansion as temperature increases. It is speculated that this hitherto unobserved behavior may be related to the different Pr-site occupancy and valence states under low vacuum which differ from those observed in air for the Ba-stoichiometric series. However, in addition to the different atmospheres of the two techniques, slight temperature variations may complicate absolute comparisons of the two sets of lattice-parameter data. The refined oxygen occupancy of the BZCY72 end-member phase decreased with increasing temperature, closely following the dehydration event.[24] In the present series, oxygen loss is also observed with increasing temperature, although the temperature at which the loss initiates is displaced to higher temperature with increasing Pr content, Figure 7.

Relatedly, lattice parameters collected in N_2 in the range 773−1173 K with SR-XRD were slightly larger than those
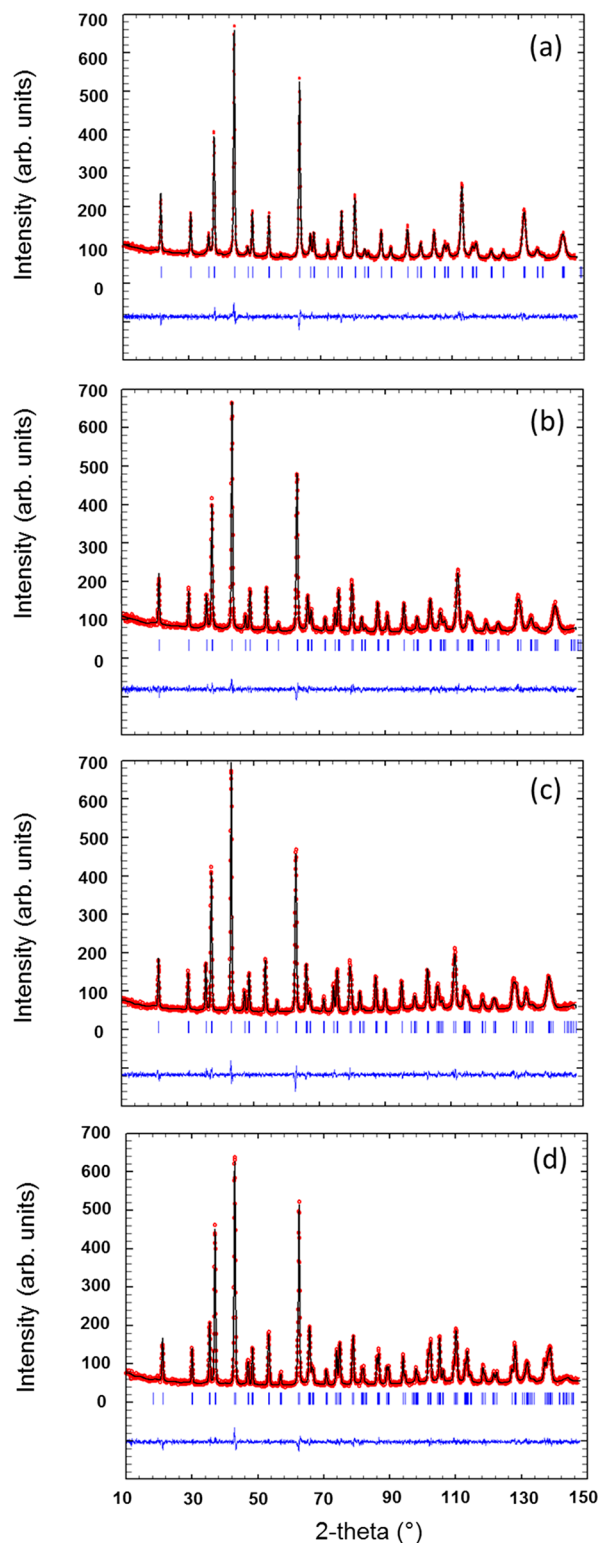
Figure 3. Experimental (circles), calculated (continuous line), and difference (continuous line at bottom of each panel) neutron diffraction patterns for x = (a) 0.2 (T = 313 K), (b) 0.4 (RT), (c) 0.6 (338 K), and (d) 0.8 (338 K). The positions of Bragg peaks are indicated by vertical bars.

collected in wet or dry air (not shown), most probably resulting from a small amount of reduction associated with oxygen loss. This behavior is discussed more fully in the context of interpretation of the electrical-conductivity data.
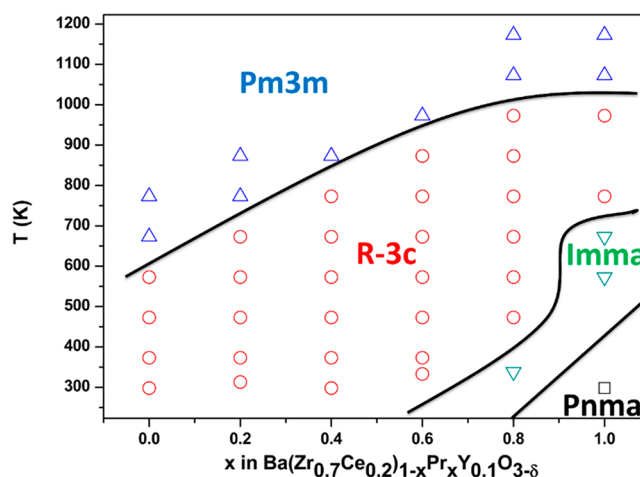
Figure 4. Phase fields of the $Ba(Zr_{0.7}Ce_{0.2})_{1-x}Pr_xY_{0.1}O_{3-\delta}$ series determined from NPD data.
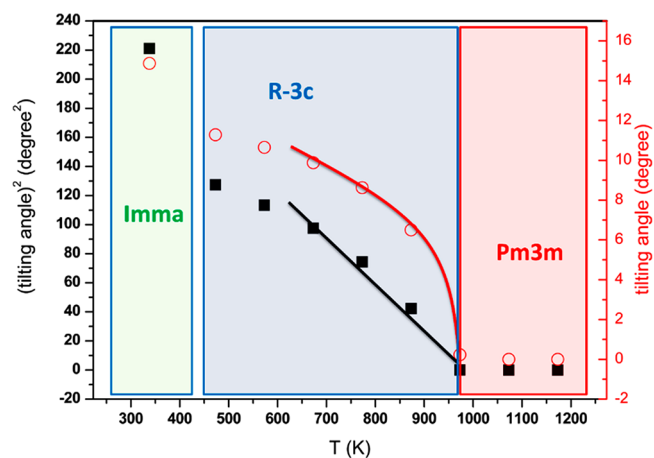
Figure 5. Square of the octahedral tilt angle (φ) of the x = 0.8 member of the $Ba(Zr_{0.7}Ce_{0.2})_{1-x}Pr_xY_{0.1}O_{3-\delta}$ series as a function of temperature (squares, primary y-axis) and φ as a function of temperature (circles, secondary y-axis).
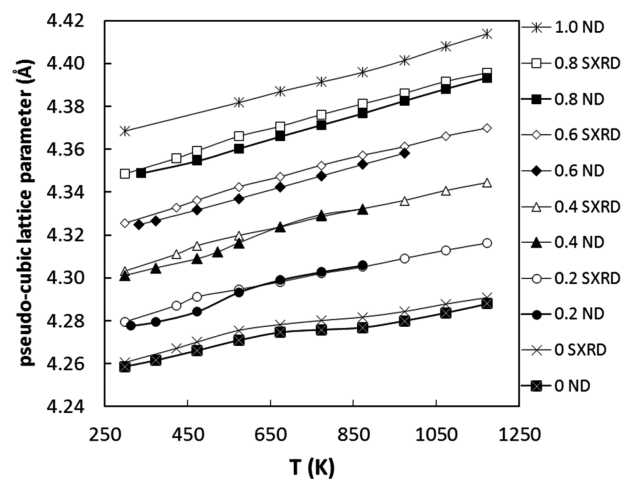

Figure 6. Pseudocubic lattice constants of the $Ba(Zr_{0.7}Ce_{0.2})_{1-x}Pr_xY_{0.1}O_{3-\delta}$ series determined from ND data on heating in low vacuum or from SR-XRD data on heating in synthetic air.

Thermal Behavior in CO_2. Thermogravimetry was performed on heating in CO_2 to provide a preliminary
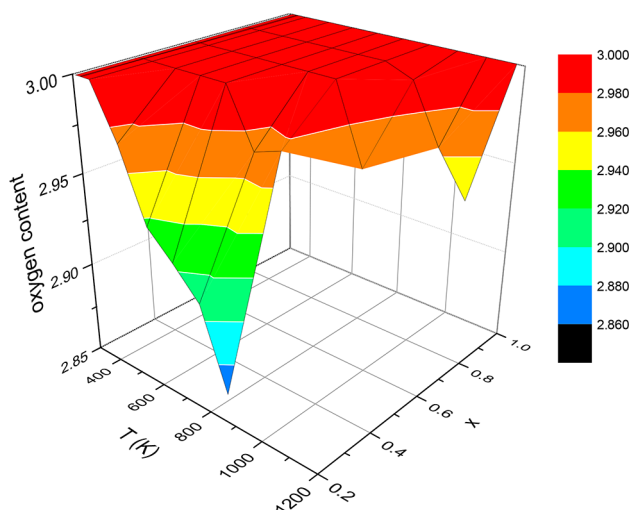
Figure 7. Schematic diagram of oxygen content as a function of temperature and Pr content (x) for the $Ba(Zr_{0.7}Ce_{0.2})_{1-x}Pr_xY_{0.1}O_{3-\delta}$ series.

comparison of stability within the series. Samples were first heated to 1173 K and cooled in synthetic air prior to heating in CO_2. The change in mass during the air cycle varied within a narrow range and did not provide a reliable indication of water content. Significant mass loss which could be attributed to reduction of Pr^{4+} or Ce^{4+} species was not observed. Mass gain was, however, observed on heating in CO_2 for $x \geq 0.6$, which increased and was displaced to lower temperatures with increasing Pr content, Figure 8.
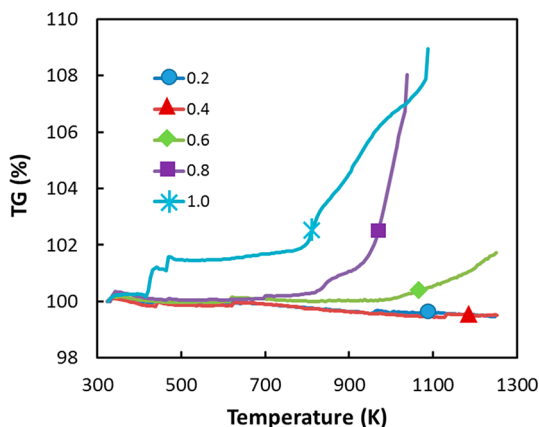

Figure 8. TGA plots of the $Ba(Zr_{0.7}Ce_{0.2})_{1-x}Pr_xY_{0.1}O_{3-\delta}$ series in 100% CO_2 with a heating rate of 5 K min^{-1}.

Significant weight gain commenced at ∼423 K for the x = 1.0 sample, reflecting the poor stability of this phase. The results are concurrent with the related $Ba(Zr_{0.7}Ce_{0.2})_{1-(x/0.9)}$-$Pr_xY_{0.1}O_{3-\delta}$ series[15] and other Pr-doped $BaZrO_3$-based systems.[12,40] In our previous paper on the Ba-stoichiometric series,[15] we attributed the poorer stability of the Pr-doped samples to the larger average B-site cation radius forming a bond in which O is a better electron donor, and to a lower Goldschmidt tolerance factor, generally associated with poorer phase stability.[41] Notably, lowering the Ba chemical potential with respect to the Ba-stoichiometric series does not have a positive effect on the phase stability in the present series.

Electrical Conductivity. Impedance spectra obtained at 573 K in wet and dry N_2 and at 1173 K in wet N_2 for the x = 0.8 composition are shown in Figure 9.
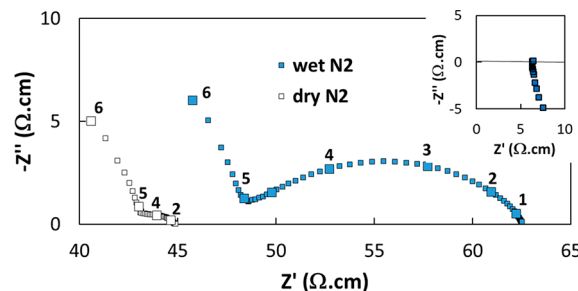

Figure 9. Impedance spectra at 573 K in wet and dry N_2, and at 1173 K in wet N_2 (inset) for the x = 0.8 composition of the $Ba(Zr_{0.7}Ce_{0.2})_{1-x}Pr_xY_{0.1}O_{3-\delta}$ series; numbers refer to $\log_{10}$ of the frequency.

At high temperature, spectra were characterized by a purely resistive process attributable to the total resistance (inset, Figure 9) in series with an autoinductive feature arising from the experimental setup, with members of lower Pr content frequently presenting a small, additional electrode response. On decreasing temperature, at least two impedance contributions could generally be identified. Figure 9 illustrates a typical response with a high-frequency feature of associated capacitance ∼1 × 10^{-9} F indicative of a grain-boundary process,[42] and a low-frequency pseudo-semicircle with calculated capacitance of approximately 1 × 10^{-4} F, attributable to electrode−material interface processes.

The temperature dependence of total conductivity of the $Ba(Ce_{0.2}Zr_{0.7})_{1-x}Pr_xY_{0.1}O_{3-\delta}$ series was determined from the impedance plots and is shown in dry air and N_2 in Figure 10a,b, respectively, with comparisons of the conductivities in the two atmospheres for selected series members shown in Figure 10d−f; corresponding activation energies are listed in Table 3.

Conductivity is raised in the low-temperature range by around 4 orders of magnitude for the later series members in comparison to BZCY72 with a concomitant decrease in activation energy in all measured atmospheres. The activation energy in dry air decreases from 1 eV for the BZCY72 phase to 0.32 eV in the series member x = 0.8; however, the Pr-rich end-member (x = 1) shows slightly higher activation energies and lower conductivity than the x = 0.8 sample, except for the highest measured temperatures in both dry air and N_2. Similar increases in conductivity with increasing Pr content are observed in the Ba-stoichiometric series, and in related $BaZrO_3$-based systems on substitution with Pr.[12,16] We recently reported transport numbers for the Pr-free BZCY72 phase,[3] which map the mixed ionic−electronic nature of conductivity in dry air and N_2. The higher conductivity in dry air in comparison to that in dry N_2 observed for the present series (Figure 10) is also consistent with a significant p-type electronic contribution to transport, reflected in the lower activation energies with increasing x (Table 3). We note that the difference between conductivity in the two dry atmospheres is greater for later series members at high temperature, suggesting a greater role of electronic transport carriers at the expense of ionic species. As also observed in the previously studied $Ba(Zr_{0.7}Ce_{0.2})_{1-(x/0.9)}Pr_xY_{0.1}O_{3-\delta}$ system,[15]
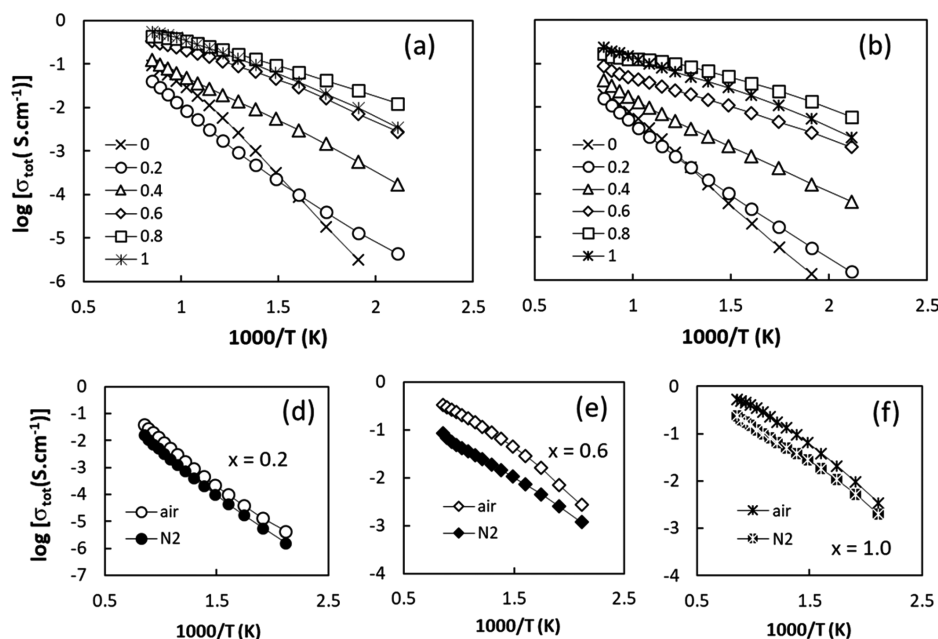
Figure 10. Arrhenius plots of total conductivity for the $Ba(Zr_{0.7}Ce_{0.2})_{1-x}Pr_xY_{0.1}O_{3-\delta}$ series in (a) dry air and (b) dry N_2. (d−f) Comparisons of conductivities in dry air and N_2 for selected compositions.

Table 3. Activation Energy (in eV) of Electrical Conductivity for $Ba(Zr_{0.7}Ce_{0.2})_{1-x}Pr_xY_{0.1}O_{3-\delta}$ as a function of Pr Concentration, in Dry and Humidified Air and N_2 Atmospheres in the Temperature Range 523−723 K

	dry		wet	
x	air	N₂	air	N₂
0	1.0	0.84	0.74	0.69
0.2	0.65	0.65	0.64	0.64
0.4	0.50	0.46	0.52	0.47
0.6	0.41	0.34	0.41	0.36
0.8	0.32	0.31	0.34	0.32
1	0.42	0.37	0.43	0.41

the conductivities in dry air and N_2 become closer at low temperature, suggesting that this is a common feature of such perovskites. The trend toward convergence in the BZCY72 end-member and Pr-lean phases in the two atmospheres at low temperature may be attributable to the higher activation energy of electron−hole conductivity with respect to oxide-ion conductivity[43,44] such that the ionic contribution to conductivity is higher at low rather than high temperatures. This has the effect that the conductivity is less affected by the oxygen activity of different atmospheres at lower temperature. A further consideration relevant to the highly electronic Pr-rich members is the higher mobility and concentration of electron holes at high temperature. Whereas the introduction of Pr in the Ba-stoichiometric series alone had the effect of reducing the oxygen-vacancy concentration, partitioning of B cations on the Ba-site also has a clear effect of lowering the oxygen-vacancy concentration, as discussed earlier (Figure 7). The enthalpy change for the oxidation reaction

$$V_o^{\cdot\cdot} + \frac{1}{2}O_2 \rightarrow O_o^\times + 2h^{\cdot} \qquad (4)$$

determined semiempirically for $BaPr_{0.9}Gd_{0.1}O_{3-\delta}$[45] indicates that, at low temperature, the formation of holes is more favorable than that of oxygen vacancies. Note that the authors

obtained positive enthalpy changes for the reverse reaction which states that eq 4 is exothermic. We may expect, therefore, that electron holes are the dominant charge balancing the acceptor dopant:

$$[Y'_{Zr}] \approx [h^{\cdot}] \qquad (5)$$

The concentration of holes is, thus, fairly constant and mainly determined by the dopant content in the low-temperature range, such that changes in oxygen partial pressure have little effect on the concentration of charge carriers. As temperature increases, however, the formation of oxygen vacancies is more favorable (eq 4 is displaced to the left) and they participate in maintaining electroneutrality (protons are considered negligible species in dry conditions):

$$[Y'_{Zr}] = 2[V_o^{\cdot\cdot}] + [h^{\cdot}] \qquad (6)$$

At high temperature, the creation of oxygen vacancies becomes the principal charge-compensation mechanism for the acceptor dopant. Concomitantly, the electronic conductivity approximates a classical power-law dependency, $\sigma_e \propto \log pO_2^{+1/4}$,[46] where the difference in conductivities in dry air and dry N_2 is much more marked than at low temperature.

The oxidation states as determined from magnetic measurements and Rietveld refinement of neutron data (Figure 7) indicate that Pr on the B-site is likely to be present almost exclusively in the IV oxidation state. The origin of the electronic conductivity in this and the Ba-stoichiometric series[15] may be considered, therefore, as holes residing in the oxygen band, since mixed Pr valence states on the perovskite B-site may be discounted as the origin of the electronic hopping. Accordingly, the source of electronic conductivity of $BaPrO_3$ in oxidizing conditions has been modeled as O^- species.[47] A similar situation arises in the current Ba-deficient system because although the partitioning mechanism produces Pr^{3+} (eq 2), it is hosted in the A position of the perovskite, preventing the hopping of holes between different Pr species.

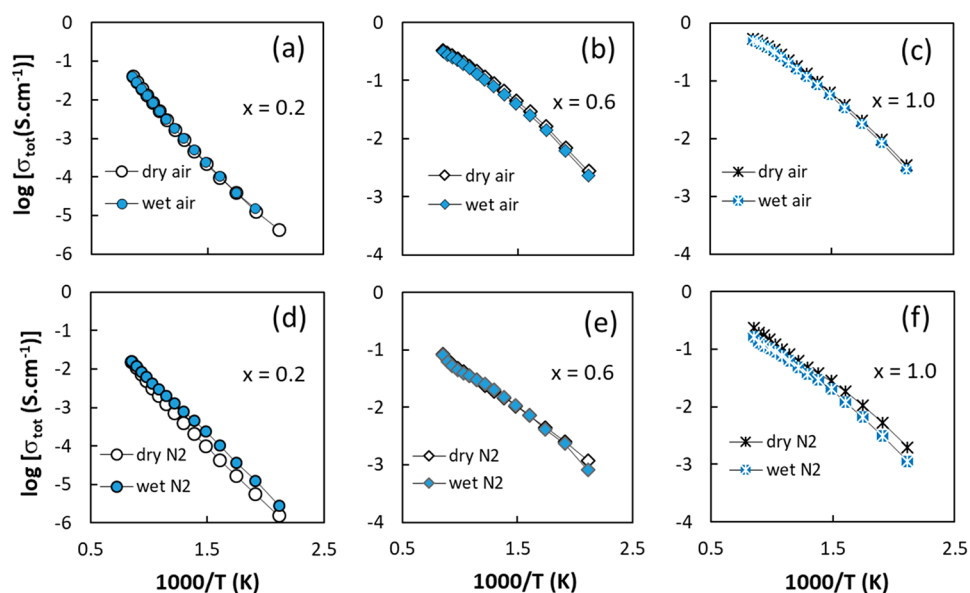Arrhenius plots in wet and dry air and N_2 for selected samples are shown in Figure 11.

Figure 11. Comparisons of temperature dependencies of total conductivity for selected members of the $Ba(Zr_{0.7}Ce_{0.2})_{1-x}Pr_xY_{0.1}O_{3-\delta}$ series in dry and wet air (a–c), and dry and wet N_2 (d–f).

The difference in conductivity between wet and dry air is marginal for the x = 0.2 sample (Figure 11a), due to the dominating character of the electron–hole component at such high oxygen activities. Analogous to the Ba-stoichiometric system, with increasing Pr content, increasingly lower conductivity values are observed in wet air in comparison to dry (Figure 11b,c), consistent with the partial consumption of the dominating electron–hole species by less mobile protons according to the following defect reaction:

$$\frac{1}{2}H_2O + h^{\cdot} + O_o^{\times} \Leftrightarrow OH_o^{\cdot} + \frac{1}{2}O_2 \tag{7}$$
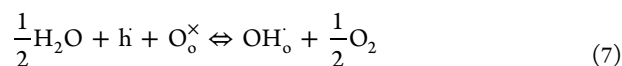
The effect of lowering pO_2 in wet conditions for the Pr-lean x = 0.2 sample (Figure 11a,d) is to lower the electron–hole concentration (eq 4) such that the oxygen-vacancy content and, in turn, the proton content are significantly higher in the wet atmosphere in comparison to the dry atmosphere. In contrast, comparison of the Pr-rich phases in wet and dry N_2 (Figure 11e,f) indicates a similar behavior to that observed in air (Figure 11b,c), with electron–holes predominating transport irrespective of water content.

CONCLUSIONS

The technologically relevant BZCY72–BaPrO$_3$ system exhibits a wide interval of Ba substoichiometry, with a complete solid-solution forming in the range $Ba(Zr_{0.7}Ce_{0.2})_{1-x}Pr_xY_{0.1}O_{3-\delta}$ ($0 \leq x \leq 1$) with various distortions of the perovskite structure. Symmetry changes in the sequence $Pnma \rightarrow Imma \rightarrow R\bar{3}c \rightarrow Pm\bar{3}m$ were determined by Rietveld refinement of neutron diffraction and synchrotron radiation X-ray diffraction, with greater octahedral tilting observed for higher Pr content and lower temperature in accordance with lowering of the tolerance factor. The refinements and magnetic-susceptibility data indicate that Ba substoichiometry is compensated for by partitioning of multiple B-site cations on the perovskite A-site with concomitant increase in the oxygen content. The lower tolerance factor with greater Pr content and more ionic B–O bonds is likely to cause the poor stability of Pr-rich phases in CO_2.

Pr substitution substantially increases electrical conductivity via electron–hole formation, as indicated by high refined oxygen contents for all series members and displacement of the temperature of oxygen loss to higher values with increasing Pr content. However, for lower Pr contents, as for the BZCY72 end-member, oxygen-vacancy formation is competitive with hole formation such that protons contribute significantly to transport in wet, more reducing atmospheres. The mixed ("triple") conductivity of solid-solution members with low Pr contents and their better stability in comparison to Pr-rich phases render these materials promising components in composite protonic ceramic fuel cell cathodes.

AUTHOR INFORMATION

Corresponding Author

*E-mail: mather@icv.csic.es. Phone: 0034 917355840.

ORCID ⓘ

Ulises Amador: 0000-0002-4412-2419
Duncan P. Fagg: 0000-0001-6287-9223
Domingo Pérez-Coll: 0000-0001-5331-2516
Glenn C. Mather: 0000-0003-0779-4619

Notes

The authors declare no competing financial interest.

Kermorvant and Alexandre Bosser of the IUT, University of Rennes (France), for assistance.

■ REFERENCES

(1) Robinson, S.; Manerbino, A.; Grover Coors, W.; Sullivan, N. P. Fabrication and Performance of Tubular, Electrode-Supported $BaCe_{0.2}Zr_{0.7}Y_{0.1}O_{3-\delta}$ Fuel Cells. *Fuel Cells* **2013**, *13* (4), 584.

(2) Vasileiou, E.; Kyriakou, V.; Garagounis, I.; Vourros, A.; Stoukides, M. Ammonia Synthesis at Atmospheric Pressure in a $BaCe_{0.2}Zr_{0.7}Y_{0.1}O_{2.9}$ Solid Electrolyte Cell. *Solid State Ionics* **2015**, *275*, 110−116.

(3) Heras-Juaristi, G.; Pérez-Coll, D.; Mather, G. C. Temperature Dependence of Partial Conductivities of the $BaZr_{0.7}Ce_{0.2}Y_{0.1}O_{3-\delta}$ Proton Conductor. *J. Power Sources* **2017**, *364*, 52−60.

(4) Fabbri, E.; Markus, I.; Bi, L.; Pergolesi, D.; Traversa, E. Tailoring Mixed Proton-Electronic Conductivity of $BaZrO_3$ by Y and Pr Co-Doping for Cathode Application in Protonic SOFCs. *Solid State Ionics* **2011**, *202* (1), 30−35.

(5) Duan, C.; Tong, J.; Shang, M.; Nikodemski, S.; Sanders, M.; Ricote, S.; Almansoori, A.; OHayre, R. Readily Processed Protonic Ceramic Fuel Cells with High Performance at Low Temperatures. *Science* **2015**, *349* (6254), 1321−1326.

(6) Duan, C.; Hook, D.; Chen, Y.; Tong, J.; O'Hayre, R. Zr and Y Co-Doped Perovskite as a Stable, High Performance Cathode for Solid Oxide Fuel Cells Operating below 500 °C. *Energy Environ. Sci.* **2017**, *10* (1), 176−182.

(7) Xie, K.; Zhang, Y.; Meng, G.; Irvine, J. T. S. Electrochemical Reduction of CO_2 in a Proton Conducting Solid Oxide Electrolyser. *J. Mater. Chem.* **2011**, *21* (1), 195.

(8) Morejudo, S. H.; Zanon, R.; Escolastico, S.; Yuste-Tirados, I.; Malerod-Fjeld, H.; Vestre, P. K.; Coors, W. G.; Martinez, A.; Norby, T.; Serra, J. M.; Kjolseth, C. Direct Conversion of Methane to Aromatics in a Catalytic Co-Ionic Membrane Reactor. *Science* **2016**, *353* (6299), 563−566.

(9) Antunes, I.; Mikhalev, S.; Mather, G. C.; Kharton, V. V.; Figueiras, F. G.; Alves, A.; Rodrigues, J.; Correia, M. R.; Frade, J. R.; Fagg, D. P. Site Redistribution, Partial Frozen-in Defect Chemistry, and Electrical Properties of $Ba_{1-x}(Zr,Pr)O_{3-\delta}$. *Inorg. Chem.* **2016**, *55*, 8552−8563.

(10) Fabbri, E.; Bi, L.; Tanaka, H.; Pergolesi, D.; Traversa, E. Chemically Stable Pr and y Co-Doped Barium Zirconate Electrolytes with High Proton Conductivity for Intermediate-Temperature Solid Oxide Fuel Cells. *Adv. Funct. Mater.* **2011**, *21* (1), 158−166.

(11) Wang, Z.; Liu, M.; Sun, W.; Ding, D.; Lü, Z.; Liu, M. A Mixed-Conducting $BaPr_{0.8}In_{0.2}O_{3-\delta}$ Cathode for Proton-Conducting Solid Oxide Fuel Cells. *Electrochem. Commun.* **2013**, *27*, 19−21.

(12) Magrasó, A.; Frontera, C.; Gunnæs, A. E.; Tarancón, A.; Marrero-López, D.; Norby, T.; Haugsrud, R. Structure, Chemical Stability and Mixed Proton-Electron Conductivity in $BaZr_{0.9-x}Pr_xGd_{0.1}O_{3-\delta}$. *J. Power Sources* **2011**, *196* (22), 9141−9147.

(13) Magrasó, A.; Espiell, F.; Segarra, M.; Irvine, J. T. S. Chemical and Electrical Properties of $BaPr_{0.7}Gd_{0.3}O_{3-\delta}$. *J. Power Sources* **2007**, *169* (1), 53−58.

(14) Antunes, I.; Mather, G. C.; Frade, J. R.; Gracio, J.; Fagg, D. P. Stability of $Ba(Zr,Pr,Y)O_{3-\delta}$ Materials for Potential Application in Electrochemical Devices. *J. Solid State Chem.* **2010**, *183* (12), 2826−2834.

(15) Heras-Juaristi, G.; Amador, U.; Fuentes, R. O.; Chinelatto, A. L.; Romero De Paz, J.; Ritter, C.; Fagg, D. P.; Pérez-Coll, D.; Mather, G. C. Thermal Evolution of Structures and Conductivity of Pr-Substituted $BaZr_{0.7}Ce_{0.2}Y_{0.1}O_{3-\delta}$: Potential Cathode Components for Protonic Ceramic Fuel Cells. *J. Mater. Chem. A* **2018**, *6* (13), 5324−5334.

(16) Antunes, I.; Amador, U.; Alves, A.; Correia, M. R.; Ritter, C.; Frade, J. R.; Pérez-Coll, D.; Mather, G. C.; Fagg, D. P. Structure and Electrical-Transport Relations in $Ba(Zr,Pr)O_{3-\delta}$ Perovskites. *Inorg. Chem.* **2017**, *56* (15), 9120−9131.

(17) Slater, P. R.; Fagg, D. P.; Irvine, J. T. S. Synthesis and Electrical Characterisation of Doped Perovskite Titanates as Potential Anode Materials for Solid Oxide Fuel Cells. *J. Mater. Chem.* **1997**, *7* (12), 2495−2498.

(18) Sun, Y.; Li, J.; Zeng, Y.; Amirkhiz, B. S.; Wang, M.; Behnamian, Y.; Luo, J. A-Site Deficient Perovskite: The Parent for in Situ Exsolution of Highly Active, Regenerable Nano-Particles as SOFC Anodes. *J. Mater. Chem. A* **2015**, *3* (20), 11048−11056.

(19) Azough, F.; Jackson, S. S.; Ekren, D.; Freer, R.; Molinari, M.; Yeandel, S. R.; Panchmatia, P. M.; Parker, S. C.; Maldonado, D. H.; Kepaptsoglou, D. M.; Ramasse, Q. M. Concurrent La and A-Site Vacancy Doping Modulates the Thermoelectric Response of $SrTiO_3$: Experimental and Computational Evidence. *ACS Appl. Mater. Interfaces* **2017**, *9* (48), 41988−42000.

(20) Mather, G. C.; García-Martín, S.; Benne, D.; Ritter, C.; Amador, U. A-Site-Cation Deficiency in the $SrCe_{0.9}Yb_{0.1}O_{3-\delta}$ Perovskite: Effects of Charge-Compensation Mechanism on Structure and Proton Conductivity. *J. Mater. Chem.* **2011**, *21* (15), 5764−5773.

(21) Yamazaki, Y.; Hernandez-Sanchez, R.; Haile, S. M. Cation Non-Stoichiometry in Yttrium-Doped Barium Zirconate: Phase Behavior, Microstructure, and Proton Conductivity. *J. Mater. Chem.* **2010**, *20* (37), 8158−8166.

(22) Kim, H. S.; Bae, H. B.; Jung, W. C.; Chung, S. Y. Manipulation of Nanoscale Intergranular Phases for High Proton Conduction and Decomposition Tolerance in $BaCeO_3$ Polycrystals. *Nano Lett.* **2018**, *18* (2), 1110−1117.

(23) Rodriguez-Carvajal, J. Recent Advances in Magnetic Structure Determination by Neutron Powder Diffraction. *Phys. B* **1993**, *192*, 55−69.

(24) Mather, G. C.; Heras-Juaristi, G.; Ritter, C.; Fuentes, R. O.; Chinelatto, A. L.; Pérez-Coll, D.; Amador, U. Phase Transitions, Chemical Expansion and Deuteron Sites in the $BaZr_{0.7}Ce_{0.2}Y_{0.1}O_{3-\delta}$ Proton Conductor. *Chem. Mater.* **2016**, *28*, 4292−4299.

(25) Glazer, A. M. Simple Ways of Determining Perovskite Structures. *Acta Crystallogr., Sect. A: Cryst. Phys., Diffr., Theor. Gen. Crystallogr.* **1975**, *31* (6), 756−762.

(26) Woodward, D. I.; Reaney, I. M. Electron Diffraction of Tilted Perovskites. *Acta Crystallogr., Sect. B: Struct. Sci.* **2005**, *61* (4), 387−399.

(27) Pérez-Coll, D.; Heras-Juaristi, G.; Fagg, D. P.; Mather, G. C. Transport-Number Determination of a Protonic Ceramic Electrolyte Membrane via Electrode-Polarisation Correction with the Gorelov Method. *J. Power Sources* **2014**, *245*, 445−455.

(28) Hinatsu, Y. Magnetic Susceptibility and Electron Paramagnetic Resonance Spectrum of Tetravalent Praseodymium Ions in $BaPrO_3$. *J. Solid State Chem.* **1993**, *102*, 362−367.

(29) Hinatsu, Y.; Itoh, M.; Edelstein, N. Structure and Magnetic Properties of Tetravalent Praseodymium Perovskite $SrPrO_3$. *J. Solid State Chem.* **1997**, *132* (2), 337−341.

(30) Bickel, M.; Goodman, G. L.; Soderholm, L.; Kanellakopulos, B. The Magnetic Susceptibility of Pr^{4+} in $BaPrO_3$: Evidence of Long-Range Magnetic Order. *J. Solid State Chem.* **1988**, *76*, 178−185.

(31) Goossens, D. J.; Robinson, R. A.; Telling, M. T. F. The Antiferromagnetic Structure of $BaPrO_3$. *Phys. B* **2004**, *352* (1−4), 105−110.

(32) Itoh, M.; Tezuka, K.; Wakeshima, M.; Hinatsu, Y. Magnetic Properties of $Ba_{1-x}La_xPrO_3$ and $PrLu_{1-y}Mg_yO_3$ with x and $y \leq 0.075$. *J. Solid State Chem.* **1999**, *145* (1), 104−109.

(33) Itoh, M.; Hinatsu, Y. Crystal Structures and Magnetic Properties of $Ba_{1-y}Sr_yPrO_3$ ($0 \leq y \leq 1.0$). *J. Alloys Compd.* **1998**, *264*, 119−124.

(34) Hinatsu, Y. Magnetic Properties of Tetravalent Praseodymium Perovskites $BaPrO_3$, $BaCe_yPr_{1-y}O_3$, and $Sr_yBa_{1-y}PrO_3$. *J. Solid State Chem.* **1995**, *119* (2), 405−411.

(35) D'Angelo, A. M.; Chaffee, A. L. Correlations between Oxygen Uptake and Vacancy Concentration in Pr-Doped CeO_2. *ACS Omega* **2017**, *2* (6), 2544−2551.

(36) Kruth, A.; Mather, G. C.; Jurado, J. R.; Irvine, J. T. S. Anomalous Variations of Unit Cell Parameters with Composition in Proton Conducting, $ACeO_3$-Type Perovskite Solid Solutions. *Solid State Ionics* **2005**, *176* (7−8), 703−712.

(37) Howard, C. J.; Kennedy, B. J.; Chakoumakos, B. C. Neutron Powder Diffraction Study of Rhombohedral Rare-Earth Aluminates and the Rhombohedral to Cubic Phase Transition. *J. Phys.: Condens. Matter* **2000**, *12* (4), 349−365.

(38) Hiraiwa, C.; Han, D.; Kuramitsu, A.; Kuwabara, A.; Takeuchi, H.; Majima, M.; Uda, T. Chemical Expansion and Change in Lattice Constant of Y-Doped $BaZrO_3$ by Hydration/Dehydration Reaction and Final Heat-Treating Temperature. *J. Am. Ceram. Soc.* **2013**, *96* (31922), 879−884.

(39) Andersson, A. K. E.; Selbach, S. M.; Knee, C. S.; Grande, T. Chemical Expansion Due to Hydration of Proton-Conducting Perovskite Oxide Ceramics. *J. Am. Ceram. Soc.* **2014**, *97*, 2654−2661.

(40) Magrasó, A.; Solans, X.; Irvine, J. T. S.; Segarra, M. Preparation of Stabilized Gd-Doped $BaPrO_3$ Materials by Zr Substitution. *Ceram. Int.* **2009**, *35* (5), 1819−1827.

(41) Yokokawa, H.; Kawada, T.; Dokiya, M. Thermodynamic Regularities in Perovskite and K_2NiF_4 Compounds. *J. Am. Ceram. Soc.* **1989**, *72* (1), 152−153.

(42) Irvine, J. T. S.; Sinclair, D. C.; West, A. R. Electroceramics: Characterization by Impedance Spectroscopy. *Adv. Mater.* **1990**, *2* (3), 132−138.

(43) Song, S.-J.; Wachsman, E. D.; Dorris, S. E.; Balachandran, U. Electrical Properties of P-Type Electronic Defects in the Protonic Conductor $SrCe_{0.95}Eu_{0.05}O_{3-\delta}$. *J. Electrochem. Soc.* **2003**, *150* (6), A790−A795.

(44) Sherafat, Z.; Paydar, M. H.; Antunes, I.; Nasani, N.; Brandão, A. D.; Fagg, D. P. Modeling of Electrical Conductivity in the Proton Conductor $Ba_{0.85}K_{0.15}ZrO_{3-\delta}$. *Electrochim. Acta* **2015**, *165*, 443−449.

(45) Magrasó, A.; Haugsrud, R.; Segarra, M.; Norby, T. Defects and Transport in Gd-Doped $BaPrO_3$. *J. Electroceram.* **2009**, *23* (1), 80−88.

(46) Ricote, S.; Bonanos, N.; Marco de Lucas, M. C.; Caboche, G. Structural and Conductivity Study of the Proton Conductor $BaCe_{(0.9-x)}Zr_xY_{0.1}O_{(3-\delta)}$ at Intermediate Temperatures. *J. Power Sources* **2009**, *193* (1), 189−193.

(47) Stokes, S. J.; Islam, M. S. Defect Chemistry and Proton-Dopant Association in $BaZrO_3$ and $BaPrO_3$. *J. Mater. Chem.* **2010**, *20* (30), 6258−6264.